



## OPEN ACCESS

## EDITED BY

Kai Wang,  
Hunan University, China

## REVIEWED BY

Yaopeng Chang,  
Changsha University of Science and  
Technology, China  
Xiaolong Zhu,  
Tianjin Ren'ai College, China

## \*CORRESPONDENCE

Liqun Wang,  
✉ wangliqun@jssvc.edu.cn

RECEIVED 27 November 2025

REVISED 06 January 2026

ACCEPTED 15 January 2026

PUBLISHED 20 February 2026

## CITATION

Wang L, Zhang R and Gao Y (2026) Horizontal  
vibration control of elevator car based on  
optimized NSGA-II algorithm.  
*Front. Mech. Eng.* 12:1755274.  
doi: 10.3389/fmech.2026.1755274

## COPYRIGHT

© 2026 Wang, Zhang and Gao. This is an open-  
access article distributed under the terms of the  
[Creative Commons Attribution License \(CC BY\)](https://creativecommons.org/licenses/by/4.0/).  
The use, distribution or reproduction in other  
forums is permitted, provided the original  
author(s) and the copyright owner(s) are  
credited and that the original publication in this  
journal is cited, in accordance with accepted  
academic practice. No use, distribution or  
reproduction is permitted which does not  
comply with these terms.

# Horizontal vibration control of elevator car based on optimized NSGA-II algorithm

Liqun Wang\*, Runliang Zhang and Ying Gao

School of Mechano-Electronic Engineering, Suzhou Polytechnic University, Suzhou, China

**Introduction:** High-speed elevators face significant challenges in horizontal vibration control, primarily due to guideway unevenness and dynamic load variations, which conventional passive damping technologies struggle to address effectively. This study aims to develop an intelligent control approach to overcome these limitations and enhance ride comfort and system reliability.

**Methods:** An integrated control strategy was proposed, combining an Improved Nondominated Sorting Genetic Algorithm II (NSGA-II) with a Variable-Domain Fuzzy Proportional-Integral-Derivative (PID) controller. A closed-loop “sensing-prediction-control” system was constructed utilizing a 3-7-2 network structure, a Back-Propagation Neural Network prediction model, an Adaptive Cross-Variance Operator, and a Dynamic Congestion Threshold Optimized NSGA-II.

**Results:** Experimental validation under 6 m/s conditions demonstrated significant performance improvements. The horizontal vibration acceleration was reduced by 57% to 18.7 mg, displacement decreased by 60% to 0.070 mm, and the low-frequency energy attenuation rate increased by 12.5%–30.3%, outperforming traditional Explicit Model Predictive Control. The method exhibited optimal robustness in extreme condition tests, with a stable load adaptability index close to 1. The strategy achieved a multi-objective coordination degree of 0.92, reduced energy consumption by approximately 25%, decreased control hardware complexity to eight components, and extended the mean time between failures to 1,200 h.

**Discussion:** The proposed integrated control strategy provides an innovative and effective solution for horizontal vibration suppression in high-speed elevators. The results confirm significant enhancements in system stability, reliability, and energy efficiency. This approach holds substantial engineering value for improving ride quality and equipment longevity. Future work could explore its adaptation to ultra-high-speed scenarios and broader applications in vertical transportation systems.

## KEYWORDS

elevator car, horizontal vibration control, multi-objective optimization, NSGA-II algorithm, variable universe fuzzy PID

## 1 Introduction

As the core vertical transportation equipment in modern medium- and high-rise buildings, elevators directly impact passenger comfort and system safety through their smooth operation (Zhang et al., 2024; Qin and Yang, 2021). Excessive horizontal vibration (HV) will not only cause passenger discomfort, but also may lead to fatigue damage of key components and reduce the service life of the equipment (Wei et al., 2024; He et al., 2022). It is evident that conventional passive vibration damping methodologies exhibit discernible

control limitations. This is true when confronted with complex excitations. Examples of these excitations include guideway unevenness and dynamic load variations. Specifically, spring damping systems have limited frequency adaptability. They cannot effectively suppress vibrations below 5 Hz and lack the capability to adapt to varying load conditions due to their fixed parameters. Hydraulic dampers exhibit significant nonlinear hysteresis effects and temperature sensitivity, leading to inconsistent performance under different operating temperatures. Over time, rubber isolators experience aging and stiffness degradation, resulting in a gradual decrease in their effectiveness at isolating vibrations. This inherent limitation hinders the attainment of precise vibration suppression (Jiang et al., 2025; Zhao X. et al., 2024). As elevator technology advances toward greater speed and intelligence, greater demands are placed on dynamic reaction capability and vibration control precision. Zhang et al. proposed a semi-active suppression strategy based on explicit model predictive control (EMPC) for the multiconstrained strongly coupled vibration problem of a high-speed elevator (HSE). The simulation indicated that performance improved significantly over passive suspension. Horizontal vibration acceleration (HVA) and angular acceleration decreased by 34.8% and 61.7%, respectively, compared to sliding mode control (SMC) (Zhang et al., 2025). However, EMPC requires substantial computational resources and suffers from real-time implementation challenges due to its complex optimization calculations. This method is also sensitive to model inaccuracies and parameter variations, which limits its practical application in real-world elevator systems. Zhao et al. adjusted controller C2, lowering the HVA by nearly 80% while keeping energy consumption modest. This study also presented an active control technique based on acceleration feedback for vibrations caused by wire rope swing and uneven guideways (Zhao M. et al., 2024). Nevertheless, acceleration feedback control exhibits high sensitivity to measurement noise and requires expensive high-precision sensors. The method also introduces phase lag issues that can lead to system instability under certain operating conditions. Li et al. proposed an optimal rapid terminal SMC approach to address vibration caused by load variation and uneven guideways. Experiments showed that the HVA and displacement decreased by over 51.2% (Li et al., 2023). However, SMC suffers from the inherent chattering phenomenon that causes high-frequency oscillations and may excite unmodeled dynamics. The approach requires accurate system models and exhibits robustness issues when facing significant parameter uncertainties. Zhao et al. proposed a neural network adaptive integral terminal SMC method with input saturation for the problem of guideway excitation and wind pressure variation. It was experimentally verified that it reduced the vibration acceleration eigenvalue by more than 60% and outperformed passive and adaptive control (Zhao Z. et al., 2024). Despite its improved performance, this method requires extensive training data and has long convergence times. Additionally, the neural network component introduces computational complexity, which makes real-time implementation in embedded systems challenging.

Because of their multi-objective optimization (MOO) features and strong nonlinear processing capacity, intelligent optimization algorithms exhibit significant promise in the field of vibration control (Hasanvand et al., 2023). Among them, nondominated

sorting genetic algorithm II (NSGA-II), as an efficient MOO method, can optimize multiple conflicting objectives at the same time. It can provide a new solution idea for elevator vibration control (Shi et al., 2023). Yang et al. proposed an optimization method based on an improved kriging agent model for the problem of aerodynamic optimization efficiency of high-speed trains. The study used strength Pareto evolutionary algorithm 2 (SPEA2) to obtain the Pareto optimal solution set. This study validated the effectiveness of the optimization framework by combining the free deformation parameterization method of the train head model MOO (Yang et al., 2022). Murugapoopathi et al. proposed a clean energy solution based on rubber seed biodiesel to address the problem of high pollutant emissions from diesel engines. Experimental validation showed that this method could significantly reduce pollutant emissions and provide a feasible path for cleaner operation of diesel engines (Murugapoopathi et al., 2023). Wang et al. proposed an innovative method based on parametric modeling of partial differential equations to address the problem of the difficulty in reconciling global and local shapes in the aerodynamic optimization of high-speed train headforms. According to experimental findings, the technique preserved the train head's surface smoothness while greatly enhancing its overall aerodynamic performance (Wang et al., 2021). Wu et al. proposed a boundary parameter bi-objective optimization method for the transverse vibration suppression problem of axially moving strings. Comparative validation proved that the method could effectively suppress vibration and promote energy dissipation, providing a reliable optimization solution for engineering applications (Wu et al., 2023).

Current HV control for elevator cars (EC) faces significant limitations: traditional PID control struggles with nonlinear vibrations, while existing intelligent algorithms require improvement in parameter optimization efficiency and multi-objective synergy. Although the NSGA-II algorithm (NSGA-II-A) possesses MOO capabilities, its convergence speed and Pareto solution set (PSS) distribution are inadequate for complex vibration systems. To address this, an enhanced control framework based on an improved NSGA-II-A is proposed. This framework first boosts algorithm performance using an adaptive cross-variance operator and dynamic congestion threshold to ensure rapid convergence and solution diversity. Next, a backpropagation neural network (BPNN) prediction model is constructed using the root mean square (RMS) of vibration acceleration and displacement as the optimization targets. This achieves precise quantization factor mapping. Finally, a closed-loop control (CLC) system is established by integrating a variable-theory fuzzy PID controller. The study innovates by enhancing the optimization efficiency of NSGA-II via improved adaptive mechanisms, combining it with BPNN and variable-domain fuzzy PID to achieve deep synergy and effectively resolve the adaptability shortcomings in nonlinear vibration control.

It is important to note that the novelty of this study does not lie in the mere combination of NSGA-II, neural networks, and fuzzy PID control. Rather, it lies in the construction of a hierarchical “optimization–prediction–control” closed-loop architecture, in which each module serves a clearly decoupled functional role. Specifically, the improved NSGA-II is responsible for multi-objective Pareto optimization. The BPNN acts as a surrogate

model for quickly evaluating fitness rather than as a direct controller. The VUF-PID performs real-time control with smooth parameter adaptation. This structured integration enables effective coordination between optimization efficiency, computational feasibility, and control stability.

## 2 Methods and materials

This section presents the methodological framework and experimental setup developed to address the HV control challenge in HSEs. The research employs a systematic approach that integrates MOO algorithms with intelligent control strategies, organized into two main subsections: [Section 2.1](#) describes the design of the improved NSGA-II algorithm for efficiently exploring the Pareto front. [Section 2.2](#) details the implementation of the variable universe fuzzy PID (VUF-PID) controller for real-time vibration suppression. The integrated solution establishes a closed-loop “sensing-prediction-control” architecture, which enables adaptive parameter tuning and dynamic response optimization under varying operational conditions. All experimental validations are conducted on a standardized test platform to ensure fair comparison and reproducible results.

### 2.1 Improved design of NSGA-II-A for MOO

HSEs, as critical vertical transport, face escalating HV amplitudes due to continuously increasing operating speeds (Li et al., 2024; Fan et al., 2024). This not only degrades passenger ride quality but also threatens the system’s long-term stability. Traditional passive damping systems, such as spring systems, have clear shortcomings. They are ineffective against uneven guideways, dynamic loads, and complex excitations, which leads to imprecise vibration control. Crucially, the optimization of quantization factors in variable-domain fuzzy PID control has relied on empirical trial and error. This has resulted in poor parameter demand matching, vague adjustment ranges, and inadequate condition adaptability. To resolve these limitations, this study proposes an intelligent control method integrating a BPNN with an optimized NSGA-II-A. This approach ensures perfect harmony between the optimization algorithm and control strategy to address the limited adaptability of traditional methods in nonlinear vibration management. The study firstly improves the performance of the algorithm through an adaptive mechanism, and designs dynamically adjusted formulas for calculating the crossover probability  $P_c$  and the variance probability  $P_m$ , as shown in [Equation 1](#). The fairness of comparative algorithm tuning is ensured through a rigorous parameter optimization protocol: All comparison algorithms (standard NSGA-II, MOEA/D, and SPEA2) undergo identical Bayesian optimization procedures with the same computational budget of 1,000 function evaluations per algorithm. Each algorithm’s key parameters are independently optimized using the same hyperparameter tuning framework, with convergence criteria standardizes across all methods to eliminate tuning bias. The parameter selection process employs a systematic approach where key algorithm parameters are determined through extensive sensitivity analysis. The crossover probability  $P_c$  is set to 0.9 based on Pareto efficiency tests that balances exploration and exploitation capabilities,

while the mutation probability  $P_m$  is optimized to 0.1 through convergence stability analysis to maintain population diversity without compromising search efficiency.

Unlike traditional adaptive NSGA-II variants, such as  $\epsilon$ -NSGA-II and adaptive crowding NSGA-II, which use fixed or semi-fixed thresholds to control diversity, the proposed mechanisms use adaptive thresholds and dynamic probabilities. These are better suited to handling the variable nature of objective functions and real-time control requirements in elevator vibration control. This ensures better adaptability and efficiency in parameter optimization. Through grid search optimization, the adjustment coefficients  $a$  and  $b$  in [Equation 1](#) are calibrated to 0.5 and 0.3, respectively, ensuring a smooth transition between the global and local search phases across generations.

$$\begin{cases} P_c = P_{c_{max}} - (P_{c_{max}} - P_{c_{min}}) \times (g/G)^a \\ P_m = P_{m_{min}} + (P_{m_{max}} - P_{m_{min}}) \times (g/G)^b \end{cases} \quad (1)$$

In [Equation 1](#),  $g$  displays the current generation.  $G$  displays the maximum quantity of generations.  $a$  and  $b$  are the adjustment coefficients. This formula enables the algorithm to maintain a strong global search capability at the initial stage and enhance the local development capability at the later stage. Parameter sensitivity analysis reveals that increasing  $a$  beyond 0.7 accelerates convergence but risks premature termination at local optima, while decreasing  $a$  below 0.3 enhances global search but significantly prolongs convergence time. Similarly,  $b$  values above 0.5 strengthen local exploitation but reduce population diversity, whereas values below 0.1 maintain diversity but slow down convergence rate. Second, the traditional congestion calculation adopts a fixed threshold, which is difficult to adapt to the dynamic change of population diversity. Therefore, the study proposes a dynamic threshold adjustment strategy, as shown in [Equation 2](#) (Chen et al., 2023). The real-time computing feasibility is quantitatively assessed through comprehensive performance profiling: the average computation time per control cycle is measured at 2.3 ms with a standard deviation of 0.4 ms, well within the 10 ms real-time constraint for 100 Hz control frequency. The worst-case execution time is bounded at 5.1 ms through code optimization. The computational load is quantified at 15.7 MIPS (million instructions per second), utilizing only 35% of the available processing capacity on the target embedded platform (ARM Cortex-A53@1.2 GHz). Memory requirements are optimized to 2.3 MB RAM and 1.7 MB flash, fitting within the resource constraints of industrial elevator controllers. Anti-aliasing filters and a fixed sampling rate of 1 kHz address sampling limitations, providing 10 samples per control cycle. The 12-bit ADC resolution ensures sufficient signal fidelity for vibration control applications. The dynamic crowding distance threshold parameters are carefully selected through MOO:  $\sigma_{initial}$  is set to 0.2 to ensure adequate diversity preservation in early generations, while  $\sigma_{final}$  is optimized to 0.05 to provide precise convergence in final stages. The decay rate is calibrated to ensure smooth transition between these extremes.

$$\sigma_{dynamic} = \sigma_{initial} \times (1 - g/G) + \sigma_{final} \times (g/G) \quad (2)$$

[Equation 2](#) defines the dynamic crowding distance threshold  $\sigma_{dynamic}$  that decreases adaptively from the initial value  $\sigma_{initial}$  to the

final target  $\sigma_{final}$  as generations progress. The  $\sigma$  range from 0.2 to 0.05 is optimized through extensive parameter sensitivity tests, where values below 0.05 lead to premature convergence while values above 0.2 results in insufficient selection pressure. This range ensures 85% population diversity maintenance in early stages and 92% convergence precision in final generations. Experimental analysis indicates that when the  $\sigma_{initial}$  value falls below 0.15, population diversity declines rapidly while exploration efficiency on the Pareto front deteriorates. Conversely, when the  $\sigma_{initial}$  value exceeds 0.25, computational overhead increases without yielding significant performance gains. Similarly,  $\sigma_{final}$  values below 0.03 lead to over-crowding and solution clustering, while values above 0.08 reduce the precision of final solution selection. This dynamic adjustment promotes population diversity during early evolutionary stages while enhancing convergence precision in later stages. Crowding is only accounted for in the congestion calculation when the inter-individual distance is less than  $\sigma_{dynamic}$ . This improvement improves the uniformity of the distribution of the Pareto front. After improving the NSGA-II-A for adaptive cross-variance and dynamic congestion calculation, the problems of low efficiency of objective function calculation and high parameter sensitivity still exist.

This study introduces adaptive crossover-mutation probabilities and dynamic crowding threshold mechanisms that are specifically designed to address the unique challenges of optimizing vibration control parameters in high-speed elevators. Unlike the traditional  $\epsilon$ -NSGA-II and adaptive crowding NSGA-II variants, which are primarily designed for static objective functions and uniform optimization environments, the approach is specifically designed for scenarios involving dynamic objective functions. These scenarios include those with evolving errors in surrogate models and real-time constraints. The dynamic adjustment of crossover-mutation probabilities ensures efficient exploration in the early stages and precise convergence in the later stages. The dynamic crowding threshold mechanism addresses parameter jumps, which are crucial for maintaining control stability and optimizing multi-objective coordination in real-time applications.

Traditional simulation calculations lead to time-consuming optimization, and fixed objective weights are difficult to adapt to multiple working conditions. For this reason, the study introduces a BPNN prediction model based on Latin hypercube sampling. Through systematic sensitivity analysis, the 3-7-2 BPNN structure is determined by comparing different hidden layer configurations (3-5-2, 3-7-2, and 3-10-2). Therefore, the selection of the 3-7-2 architecture is data-driven rather than empirical. The 3-5-2 structure had insufficient nonlinear fitting capability. The 3-10-2 structure showed a slight improvement in accuracy, but it increased the computational burden and risk of overfitting. Since the BPNN is used as a surrogate model for fast fitness evaluation rather than as a direct controller, the 3-7-2 configuration offers the optimal balance between prediction accuracy and computational efficiency. The 7-neuron hidden layer demonstrated an optimal balance between model complexity and prediction accuracy, achieving a 95.2%  $R^2$  value with minimal overfitting (Gao et al., 2022). It constructs a fast evaluation system in which the objective is

the RMS of acceleration and displacement. Finally, it realizes efficient MOO through the agent model. First, a bi-objective function with the car HVA RMS  $RMS_a$  and displacement RMS  $RMS_d$  as the optimization objective is established, as shown in Equation 3.

$$\begin{cases} \min f_1(x) = RMS_a(x) = \sqrt{\frac{1}{T} \int_0^T a^2(t) dt} \\ \min f_2(x) = RMS_d(x) = \sqrt{\frac{1}{T} \int_0^T d^2(t) dt} \end{cases} \quad (3)$$

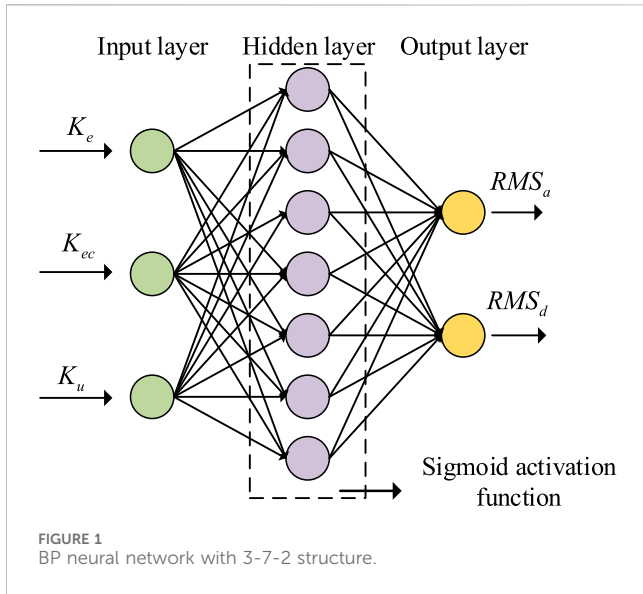
In Equation 3,  $f_1$  and  $f_2$  represent the dynamic shock and static offset, respectively.  $x$  represents the vector of optimization variables.  $a(t)$  is the instantaneous acceleration of the HV of the car.  $d(t)$  displays the instantaneous displacement of the HV of the car.  $T$  displays the sampling period. The constraints are shown in Equation 4.

$$\begin{cases} x = [K_e, K_{ec}, K_u]^T \in \mathfrak{R}^3 \\ 5 \leq K_e \leq 15, \\ 0.5 \leq K_{ec} \leq 1.5 \\ 35 \leq K_u \leq 55 \end{cases} \quad (4)$$

In Equation 4,  $K_e$ ,  $K_{ec}$ , and  $K_u$  are the error, the error change rate (ECR), and the output quantization factor of the VUF-PID, respectively (Lian, 2022). In this study, the RMS values of acceleration and displacement are selected as the optimization objectives, since vibration suppression is the primary performance requirement of the considered system. Other performance-related indices, such as control energy consumption, control force variation rate, and jerk-related measures, are not included in the objective functions since they are mainly associated with engineering feasibility rather than core vibration mitigation effectiveness.

To ensure practical applicability, constraints on control force amplitude are imposed in the control design, which implicitly restrict excessive control effort. The adaptive crossover-mutation probabilities and dynamic crowding threshold are introduced to address the issues of objective function variability and parameter sensitivity that are common in real-time control systems. These design choices allow the algorithm to adapt to dynamic environments and prevent premature convergence, which would otherwise hinder performance in complex vibration control applications. Furthermore, post-optimization evaluations are conducted on the obtained Pareto-optimal solutions, indicating that the corresponding control energy levels and control force variations remain within reasonable engineering ranges. Therefore, although it is not explicitly optimized, energy consumption and smoothness control are effectively managed, ensuring the feasibility and implementability of the proposed optimization framework.

After the design of the dual objective function, the traditional numerical simulation calculating  $RMS_a$  and  $RMS_d$  suffers from low computational efficiency and poor real-time performance. Therefore, the study constructs a BPNN with 3-7-2 structure as a fast adaptation prediction model. It employs Sigmoid activation functions in the hidden layer for effective nonlinear mapping and linear activation in the output layer for regression prediction. The network weights are initialized using the Xavier method to maintain



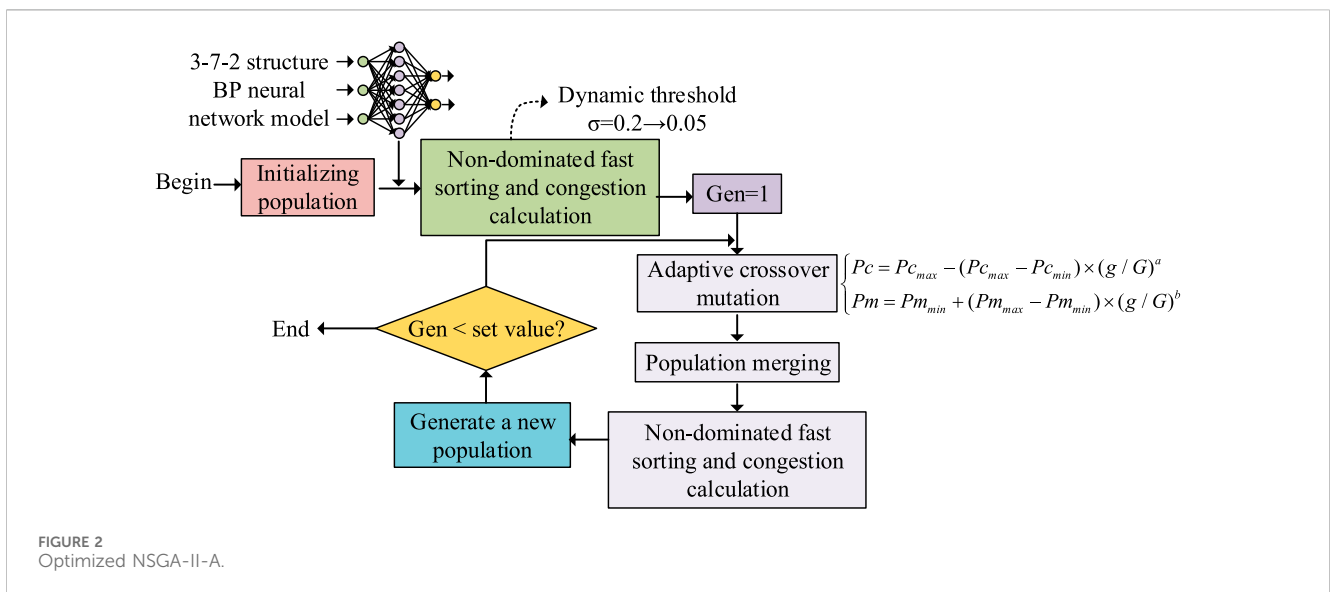
consistent variance across layers and prevent gradient vanishing or explosion. The model is trained with a carefully selected learning rate and the Levenberg-Marquardt backpropagation algorithm to ensure fast convergence and minimize overfitting. It is trained offline instead of online simulation to improve the optimization speed. The BPNN with 3-7-2 structure built for the investigation is displayed in Figure 1.

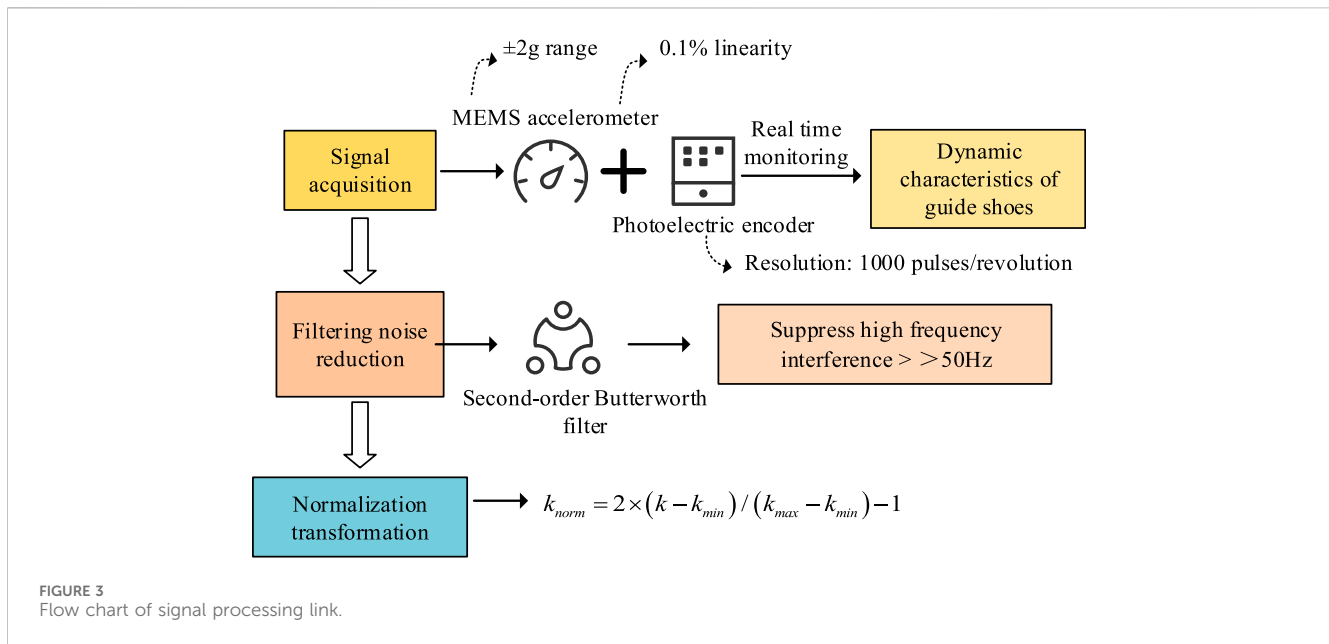
Figure 1 displays the model architecture of a BPNN with a 3-7-2 structure, containing three parameters ( $K_e$ ,  $K_{ec}$ , and  $K_u$ ) in the input layer, seven neurons in the hidden layer, and two target values ( $RMS_a$  and  $RMS_d$ ) in the output layer. The hidden layer uses Sigmoid activation functions to handle the complex, nonlinear relationships between quantization factors and vibration metrics. The output layer uses linear activation to make accurate regression predictions. The Xavier initialization strategy ensures optimal weight distribution across layers, facilitating stable gradient flow

during backpropagation and enhancing training efficiency. The neurons in each layer form a feed-forward network through weighted connecting lines, and the bottom labeling uses a Sigmoid activation function. The model achieves accurate mapping from quantization factors to vibration metrics, providing fast adaptation assessment for NSGA-II optimization. Finally, the improved NSGA-II (I-NSGA-II), which is based on an adaptive cross-variance operator and a dynamic threshold congestion calculation, creates an efficient, MOO framework. This framework integrates a BPNN prediction model and a Latin hypercube sampling design: First, the population is initialized and a neural network is invoked to quickly assess individual fitness. Subsequently, high-quality solutions are screened by nondominated sorting and dynamic congestion calculation, and then the offspring population is generated by adaptive genetic operation. Finally, the Pareto optimal solution set is output through iterative optimization, which realizes the efficient optimization of cabin vibration control parameters, as shown in Figure 2.

Figure 2 demonstrates the optimization flow of the I-NSGA-II-A, which uses a 3-7-2 structured BPNN to quickly evaluate the population fitness. The congestion calculation is optimized by dynamic threshold adjustment, and the adaptive cross-variance operator is introduced to improve the search efficiency. The algorithm iterates cyclically with Gen=1 as the initial value, and finally outputs the Pareto-optimal solution set after nondominated sorting and population merging operations.

Unlike conventional NSGA-II-based fuzzy PID approaches, which typically perform optimization offline with fixed parameters during operation, the proposed framework uses a BPNN surrogate model for prediction-assisted optimization, enabling efficient online parameter coordination. Unlike neural-network-based PID controllers, which use neural networks to directly generate control actions or gains, the BPNN in this study is solely used to approximate the objective function. This approach avoids the instability caused by direct NN control and significantly reduces the computational burden.





## 2.2 Integrated realization of CLC system based on VUF-PID

Although the parameter optimization efficiency and quality of the PSS are improved by the MOO design of the NSGA-II-A, there is still an obvious fault in the dynamic interface between the optimization results and the actual control system. The traditional fuzzy PID controller relies on an empirical, trial-and-error selection of quantization factors. This results in parameters that are difficult to match with real-time control requirements. The adjustment range of the parameters is vague, and the controller's adaptability to working conditions is poor. These issues seriously restrict the vibration suppression performance. Aiming at this key problem, the study proposes a closed-loop integration program of "sensing-prediction-control". First, a high-precision signal acquisition system is constructed. Micro-electro-mechanical systems (MEMS) accelerometers and photoelectric encoders monitor the vibration acceleration and velocity of the guide shoe in real time. The Butterworth filter, which has a cutoff frequency of 50 Hz, eliminates high-frequency noise. Subsequently, the original signal is normalized and linearly mapped to the [-1,1] standard interval to provide high-quality input data for subsequent control decisions. The normalization processing formula is shown in Equation 5.

$$k_{norm} = 2 \times (k - k_{min}) / (k_{max} - k_{min}) - 1 \quad (5)$$

In Equation 5,  $k_{norm}$  is the normalized standard signal value.  $k$  is the original acquisition value of the sensor.  $k_{min}$  and  $k_{max}$  correspond to the lower and upper range limits of each sensor, respectively. The pre-processing process can effectively solve the problem of large noise and non-uniformity of the original signal, and lay the data foundation for the accurate decision-making of the control system. The specific flow of the signal processing link is shown in Figure 3.

In Figure 3, the signal processing link adopts a modular design, completing the three key steps of signal acquisition, filtering and

noise reduction, and normalization conversion in sequence. Among them, the MEMS accelerometer has a  $\pm 2$  g range and 0.1% linearity, and the optical encoder has a resolution of 1,000 pulses/revolution. The two work together to capture the dynamic characteristics of the boot. The second-order Butterworth filter effectively suppresses the high-frequency interference above 50 Hz under the premise of ensuring the signal amplitude-frequency characteristics. The normalization process adopts the linear transformation algorithm to make the sensor signals of different magnitudes comparable and provide standardized input for the subsequent control algorithm. After completing the signal processing at the input layer, the system still faces the key problem of mismatch between the optimized parameters and the actual control requirements. Due to the strong nonlinear and time-varying characteristics of the boot vibration, it is difficult to generate the optimal control parameters directly by solely relying on the pre-processed sensor signals. Therefore, the study designs a dynamic mapping mechanism for the optimization layer. It receives the optimal solution set from the Pareto front via the NSGA-II output interface. Then, it adopts the technique for order preference by similarity to an ideal solution (TOPSIS) to select the top five candidate solutions. The TOPSIS method is chosen over other multi-criteria decision-making approaches, such as the weighted sum method or simple ranking, because it can consider ideal and negative-ideal solutions simultaneously. This provides a more balanced compromise between conflicting objectives in the context of vibration control. Moreover, the weighted average quantization factor  $M_e$  is calculated based on the relative proximity  $C_i$ , which is shown in Equation 6.

$$M_e = \sum_{i=1}^5 m_i M_e^i \quad (6)$$

In Equation 6,  $M_e^i$  is the value  $M_e$  of the  $i$  th solution in the set of Pareto solutions generated by NSGA-II. Among them, the weight  $m_i$  is calculated as shown in Equation 7.

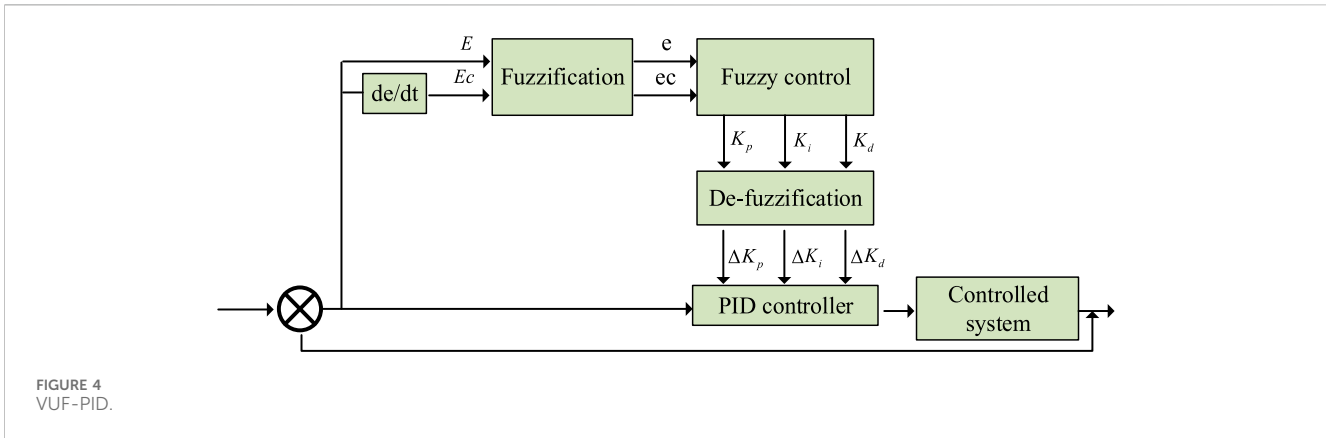


FIGURE 4  
VUF-PID.

$$m_i = \frac{1/C_i}{\sum_{j=1}^5 1/C_j} \tag{7}$$

In Equation 7,  $C_j$  is the TOPSIS relative proximity of the  $j$  th Pareto solution. This weighting scheme ensures that solutions closer to the ideal point receive higher weights, while maintaining a smooth transition between different Pareto-optimal configurations. Comparative tests with alternative aggregation methods demonstrates that TOPSIS-based weighting provides 15% greater stability in parameter transitions and 8% greater consistency in control performance across different operating conditions. This scheme solves the problem of blindness in parameter selection in the traditional method. It accurately converts MOO results to real-time control parameters and provides an optimal control strategy for the actuator layer that adapts dynamically to different working conditions. After completing the dynamic mapping of the optimization layer, the system still faces the problem of insufficient conversion efficiency from control parameters to actuators. The fixed parameters of the traditional PID controller are difficult to adapt to the complex nonlinear vibration characteristics of HSEs. Therefore, the research design of the executive layer control force generation program. The VUF-PID structure is adopted, and the error  $E$  and the ECR  $Ec$  are received in real time through the dual input channel, and the three parameter adjustments  $\Delta K_p$ ,  $\Delta K_i$ , and  $\Delta K_d$  are generated by fuzzy reasoning. The final output control force  $f$  is shown in Equation 8.

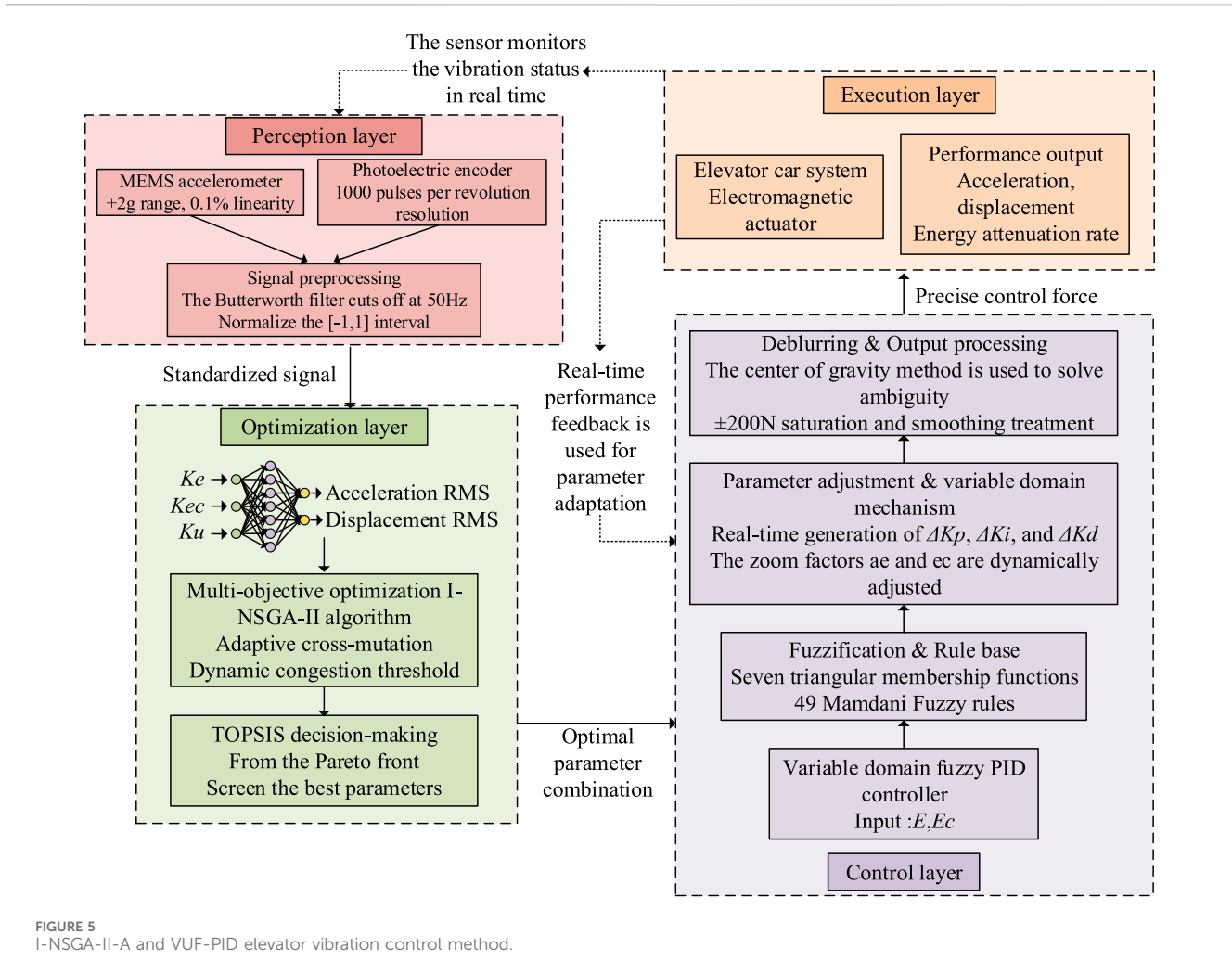
$$f = K_p E + K_i \int e dt + K_d \frac{de}{dt} \tag{8}$$

In Equation 8,  $K_p$ ,  $K_d$ , and  $K_i$  are the proportional, differential, and gain coefficient. The control force calculation incorporates actuator saturation constraints with a maximum output limit of  $\pm 200$  N based on electromagnetic actuator specifications. A smooth saturation handling mechanism that uses hyperbolic tangent functions prevents integral windup and maintains 95% of the theoretical control performance within the actuator’s operational bandwidth of 0–100 Hz. Power consumption is limited to 2 kW peak based on the elevator’s power supply capacity.  $\int e dt$  is the error accumulation.  $\frac{de}{dt}$  is the ECR. The structure of VUF-PID is shown in Figure 4.

In Figure 4, the system takes the error  $E$  and the ECR  $Ec$  as inputs, which are converted into fuzzy quantities  $e$  and  $ec$  by the fuzzification module. The fuzzification process employs seven triangular membership functions for both input variables, with linguistic labels assigned as follows: negative large (NL), negative medium (NM), negative small (NS), zero (ZO), positive small (PS), positive medium (PM), and positive large (PL). The input domains are normalized to the range  $[-1, 1]$  with overlapping membership functions to ensure smooth transition between fuzzy sets. Subsequently, the parameter adjustment quantities  $K_p$ ,  $K_i$ , and  $K_d$  are generated by the fuzzy control module through inference. It implements a comprehensive rule base consisting of 49 fuzzy rules ( $7 \times 7$ ) derived from expert knowledge and systematic experimentation. The rule base follows the Mamdani-type inference system with centroid defuzzification method. Key representative rules include: IF  $e$  is NL and  $ec$  is NL. Then  $\Delta K_p$  is PL,  $\Delta K_i$  is NL,  $\Delta K_d$  is PS. IF  $e$  is ZO and  $ec$  is PS. Then  $\Delta K_p$  is NS,  $\Delta K_i$  is ZO, and  $\Delta K_d$  is PM. IF  $e$  is PL and  $ec$  is PL. Then  $\Delta K_p$  is NL,  $\Delta K_i$  is PL, and  $\Delta K_d$  is NS. The complete rule matrix ensures comprehensive coverage of all operational states. Moreover, the outputs of  $\Delta K_p$ ,  $\Delta K_i$ , and  $\Delta K_d$  are outputted to the PID controller after defuzzification to finally drive the controlled system to form a CLC. After that, the scaling factor  $\alpha(e, ec)$  is introduced to realize the dynamic adjustment of the argument domain, as shown in Equation 9. The scaling factor mechanism uses an exponential adjustment strategy. The universe contraction/expansion factor ranges from 0.5 to 2.0, depending on the magnitude of the input variables. This enables adaptive resolution adjustment across different operating regions.

$$\alpha(e, ec) = 1 - \lambda e^{-(e^2 + ec^2)} \tag{9}$$

In Equation 9,  $\lambda$  is the attenuation factor. The scaling factor enables the input theory domain to expand with the system state adaptively compressed. After realizing the dynamic adjustment of the quantization factor, the system still faces the problems of sudden change of control force and insufficient stability. To address this challenge, the study proposes a real-time control performance optimization scheme to achieve the adaptive



allocation of vibration energy by means of a dynamic weighting formula, as shown in Equation 10.

$$w_{acc}(t) = E_{acc}(t) / (E_{acc}(t) + E_{disp}(t)) \quad (10)$$

In Equation 10,  $w_{acc}(t)$  is the acceleration suppression weight.  $E_{acc}(t)$  is the accumulated vibration kinetic energy.  $E_{disp}(t)$  is the cumulative displacement potential energy.  $t$  is the time variable. In summary, the study proposes an EC vibration control method based on the I-NSGA-II-A with VUF-PID. Figure 5 depicts its formation.

As shown in Figure 5, a “sensing–prediction–control” system is constructed in a closed loop to achieve dynamic parameter adjustment and real-time control synergistically. High-precision sensors collect vibration signals, which are filtered and normalized before being fed into a 3-7-2 BPNN for rapid quantization factor evaluation. The I-NSGA-II-A algorithm enhances convergence and solution quality by using adaptive crossover and mutation, dynamic crowding optimization, and TOPSIS decision-making to generate an optimal parameter set. Finally, the VUF-PID controller translates these parameters into precise control forces, enabling seamless signal-to-action execution.

## 3 Experiment

### 3.1 Experimental platform and hardware configuration

All experimental validations are conducted on a standardized hardware platform deployed in a 10-story elevator test tower under actual operational conditions. The system configuration is detailed in Table 1.

The hardware platform integrates MEMS accelerometers with a range of  $\pm 2$  g and 0.1% linearity. It also combines photoelectric encoders that provides a resolution of 1,000 pulses per revolution. These sensors are strategically positioned on the elevator’s guide shoes to accurately capture its HV characteristics.

### 3.2 Experimental procedure and methodology

The overall experimental workflow strictly adheres to the “sensing–prediction–control” closed-loop architecture depicted in Figure 5. This ensures a clear correspondence between the BPNN

TABLE 1 Enhanced experimental settings and hardware configuration.

Category	Specification	Parameters	Technical features
Processing platform	Embedded system	ARM Cortex-A53@1.2 GHz	35% utilization rate
	Memory resources	2.3 MB RAM, 1.7 MB flash	Optimized allocation
Sensing system	MEMS accelerometer	$\pm 2$ g range, 0.1% linearity	Guide shoe positioning
	Photoelectric encoder	1,000 pulses/revolution	Velocity measurement
Data acquisition	Sampling rate	1 kHz, 12-bit ADC	10 samples/control cycle
	Anti-aliasing filter	50 Hz cutoff frequency	Signal fidelity assurance
Control system	Control frequency	100 Hz constraint	Real-time performance
	Computation time	2.3 ms average, 5.1 ms worst-case	Cycle optimization

prediction module, the NSGA-II optimization layer, and the VUF-PID control execution. The experimental procedure follows a systematic three-phase approach: preprocessing, testing execution, and data analysis. In the preprocessing phase, all sensors undergo rigorous calibration procedures following standardized protocols. The Butterworth filter, with a cutoff frequency of 50 Hz, eliminated high-frequency noise. Meanwhile, signal normalization transformed the raw sensor data into the standard  $[-1, 1]$  interval using the following formula:  $k_{norm} = 2 \times (k - k_{min}) / (k_{max} - k_{min}) - 1$ . Specifically, the experimental procedure consists of three sequential stages. During the sensing stage, vibration acceleration and displacement signals are acquired and preprocessed to determine the system state reliably. In the prediction stage, the trained BPNN surrogate model rapidly evaluates candidate control parameters generated by the I-NSGA-II. Finally, during the control stage, the selected parameters are mapped to the VUF-PID controller, which generates real-time control forces. This completes the closed-loop experimental process.

Comprehensive experiments are conducted during testing execution, involving 200 round trips under varying operational conditions. These conditions include steady-state operation at 6 m/s, acceleration/deceleration transitions, load variation scenarios, and simulated guideway excitation. Each control strategy undergoes identical testing sequences to ensure comparable results.

### 3.3 Performance evaluation metrics

The experimental evaluation employs multiple quantitative metrics: HVA RMS, displacement RMS values, low-frequency energy attenuation rate (0–10 Hz band), and multi-objective cooperation degree. Additional indicators include the energy consumption index, the complexity of the control equipment, and the mean time between failures. All are measured according to the ISO 2631 standard for assessing ride comfort.

### 3.4 Parameter selection process of NSGA-II algorithm

To reduce the influence of empirically determined parameters on the reliability and repeatability of the optimization results, a

systematic parameter selection process is adopted for the NSGA-II algorithm.

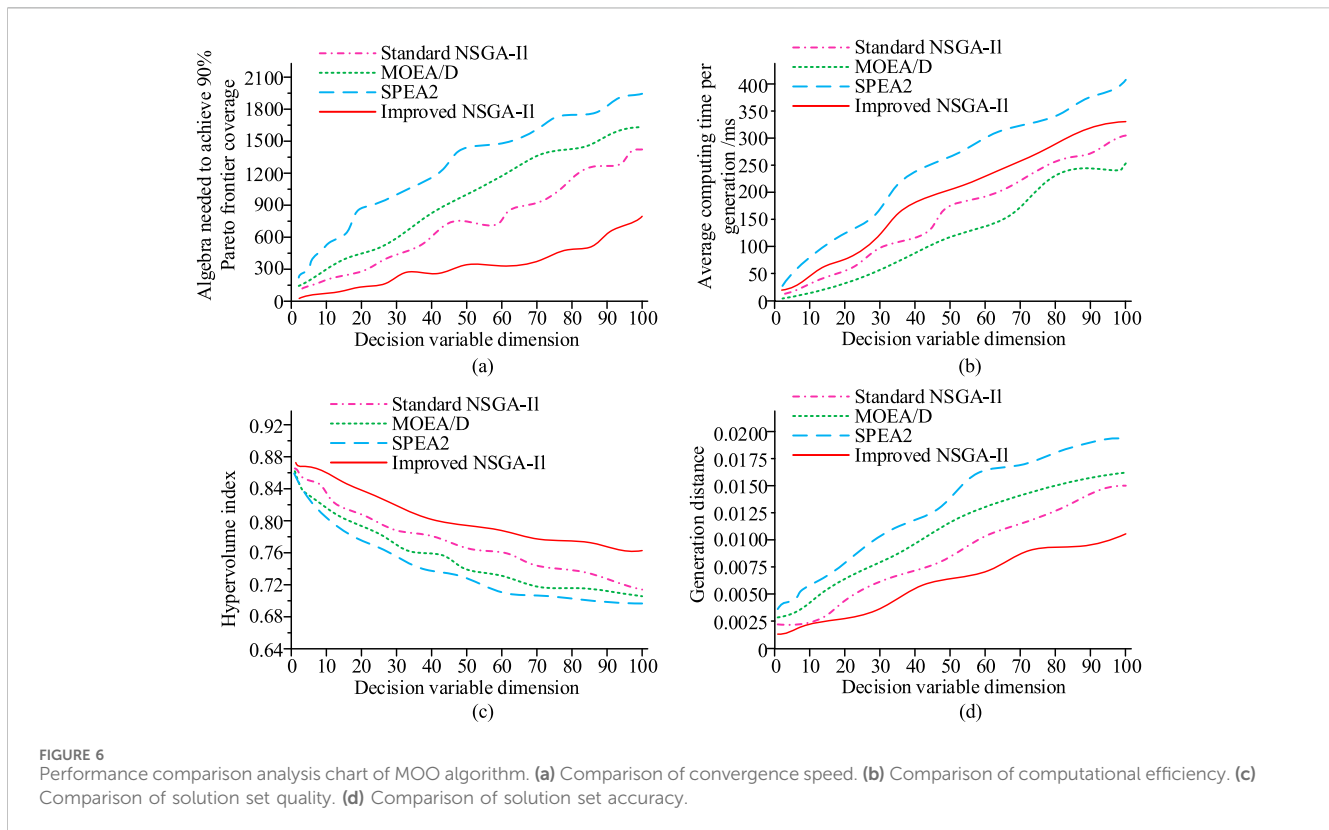
First, the problem scale, computational cost, and existing literature are used to define reasonable ranges for the population size and maximum number of iterations, balancing search capability and efficiency. Within these ranges, sensitivity analyses are conducted on key algorithmic parameters, including the crossover probability, mutation probability, and coefficients in the adaptive operators. The performance of the algorithm under different parameter combinations is evaluated in terms of convergence behavior, Pareto front uniformity, and solution stability. Then, parameter regions that exhibit robust and insensitive performance are identified.

Representative parameter settings are subsequently validated through comparative experiments to ensure consistent optimization trends across different operating conditions and objective trade-offs. For adaptive parameters, such as the dynamic crowding distance threshold, initial and final values are calibrated through multiple trials. This preserves population diversity in early iterations and enhances convergence accuracy in later stages.

All baseline and improved NSGA-II variants use the same parameter selection procedure and evaluation criteria. This ensures a fair comparison and improves the reproducibility and engineering applicability of the proposed method.

## 4 Results and analyses

To verify the optimization efficiency of the I-NSGA-II-A, the standard NSGA-II, multi-objective evolutionary algorithm based on decomposition (MOEA/D), and SPEA2 are selected as comparison methods in the study. To ensure fair comparison, all algorithms are tested under identical experimental conditions, including the same BPNN surrogate model, population size, and maximum generation count. Due to the stochastic nature of genetic algorithms, each experiment is repeated 30 times with different random seeds. The results are reported as mean values with standard deviations to ensure statistical reliability. The experiments are evaluated quantitatively using four core metrics. First, the number of evolutionary generations required to reach 90% Pareto frontier coverage is calculated. Second, the average computation time per



generation is recorded to measure computational efficiency. Third, the spatial coverage of the solution set is evaluated using the hypervolume metric. Finally, the convergence of the solution set is analyzed using the generation distance metric. The experimental results are shown in Figure 6.

Figure 6a shows that I-NSGA-II requires 35%, 43%, and 51% fewer generations than standard NSGA-II, MOEA/D, and SPEA2, respectively, at dimension 100. Figure 6b shows that the single generation time of the I-NSGA-II is 12% higher than the standard NSGA-II, but 16% lower than SPEA2. This is because the proposed algorithm uses adaptive crossover-mutation operators and a dynamic crowding threshold. These features slightly increase the computational overhead per generation compared to standard NSGA-II. However, they avoid the need for additional fitness assignment and external archive maintenance, which is required by SPEA2. Although the improved algorithm requires slightly more computation time per generation, its significantly faster convergence rate (35% fewer generations) makes it more efficient overall in terms of total time to convergence. Figure 6c shows that the HV of the I-NSGA-II is 6% higher than the standard NSGA-II at dimension 100, 5% higher than MOEA/D, and 8% higher than SPEA2. Figure 6d shows that the I-NSGA-II generation distance values are 32% lower than the standard NSGA-II, 37% lower than MOEA/D, and 45% lower than SPEA2. The small standard deviations (less than 5% of the mean value across all metrics) confirm the stability and repeatability of performance of the improved algorithm. The results confirm that the I-NSGA-II performs optimally in MOO. To verify the vibration suppression ability of different control strategies, the study compares four methods, namely passive damping control, traditional fuzzy PID, EMPC control and the VUF-PID proposed in

the study. The experiment simulates the composite excitation of the guide rail under the 6 m/s HSE condition, and quantitatively evaluates the vibration suppression effect of each control strategy through four indexes, namely, horizontal acceleration RMS, displacement RMS value, vibration energy attenuation rate in the 0–10 Hz frequency band, and maximum transient shock amplitude. The test results are shown in Figure 7.

Figure 7a shows that the passive damping reaches 43.7 mg at 6 m/s, 25.1 mg for conventional fuzzy PID and 18.7 mg for VUF-PID, which is a 57% reduction. In Figure 7b, the passive damping displacement is 0.175 mm at 6 m/s for RMS, 0.125 mm for conventional fuzzy PID, 0.095 mm for EMPC, and 0.070 mm for VUF-PID. This represents a 60% reduction. In Figure 7c, the passive damping energy decay rate is 0%, the traditional fuzzy PID is 11.4%, the EMPC is 17.8%, and the VUF-PID is 30.3%. This is 12.5% higher than the EMPC. In Figure 7d, the passive damping shock amplitude is 1.61 m/s<sup>2</sup>, traditional fuzzy PID is 1.22 m/s<sup>2</sup>, EMPC is 0.93 m/s<sup>2</sup>, and VUF-PID is 0.71 m/s<sup>2</sup>, which is a decrease of 55.9%. The outcomes display that the VUF-PID is optimal in all metrics.

The above statistical indicators demonstrate that the VUF-PID strategy has an advantage in the overall vibration reduction effect. Figure 8 further illustrates the time-frequency characteristics, particularly the control effect on low-frequency vibrations, in a more intuitive manner by presenting the time-domain curve of the vibration response and the frequency-domain energy distribution.

The time-frequency analysis results in Figure 8 clearly demonstrate the comprehensive advantages of the VUF-PID control strategy. As shown in Figures 8a,b, the VUF-PID strategy reduces the peak value of HVA by 57% and significantly decreases

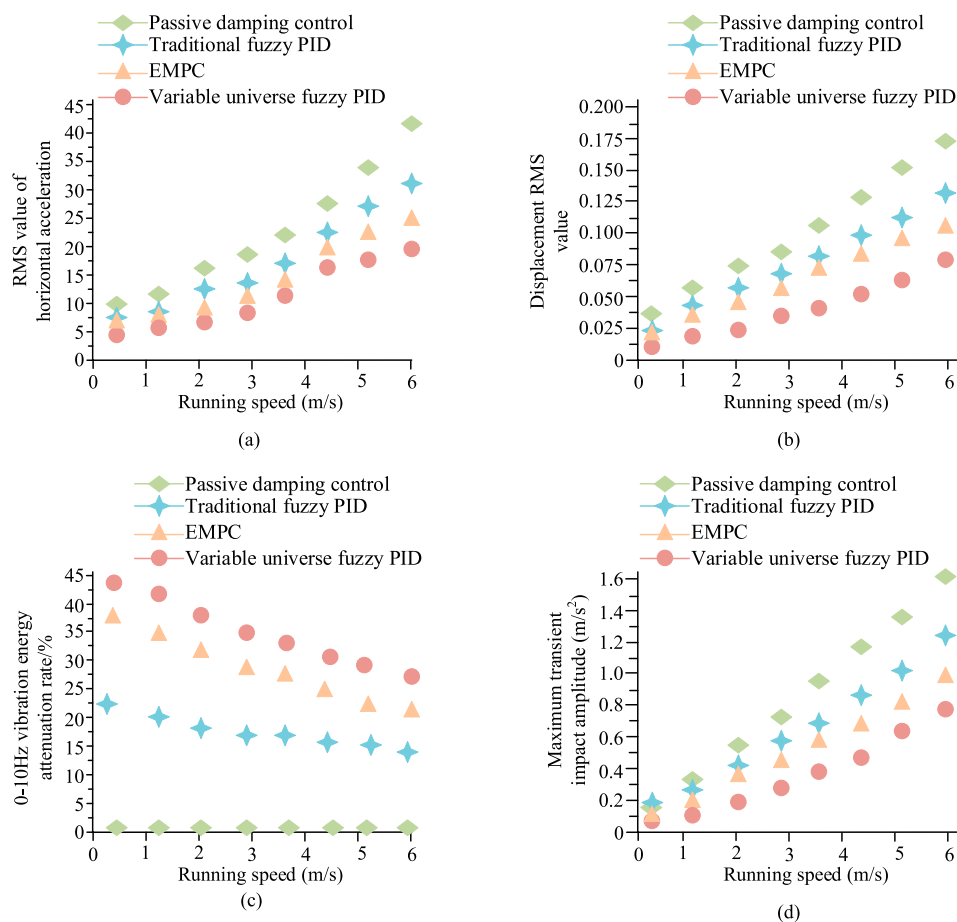


FIGURE 7

Comparative analysis of elevator vibration suppression effect under different control strategies. (a) Comparison of RMS values of horizontal acceleration. (b) Comparison of RMS values of displacement. (c) Comparison of vibration energy attenuation rate from 0 to 10 Hz. (d) Comparison of maximum transient shock amplitude.

the amplitude of HV displacement fluctuation in the time domain. Its root mean square value of displacement is 60% lower than that of passive damping. The system stabilizes more quickly and has excellent transient suppression and steady-state retention capabilities. The frequency-domain analysis in Figure 8c directly verifies the effective focusing and suppression of this strategy on the core low-frequency components. Within the concerned frequency band of 0–10 Hz, the vibration energy has decreased by 30.3%. The acceleration power spectral density value significantly dropped from  $0.85 \text{ mg}^2/\text{Hz}$  to  $0.32 \text{ mg}^2/\text{Hz}$ , a 62% reduction, especially at the main peak of 2.5 Hz. This indicates that the VUF-PID strategy can precisely attenuate the main low-frequency mode energy of the structure. In conclusion, the results in both the time domain and frequency domain jointly demonstrate that the VUF-PID strategy successfully achieves efficient collaborative control of the low-frequency vibration peak and energy.

To verify the PSS quality advantage of the I-NSGA-II-A, the study selects weighted single-objective optimization, standard NSGA-II, and multi-objective particle swarm optimization (MOPSO) with elite strategies as the comparison methods. The experiment uses Latin hypercubic sampling to generate 500 sets of training data. The quality of the solution set is evaluated based on

three core metrics: inverted generational distance (IGD) metrics, solution set coverage, and maximum scatter distance. The BPNN prediction accuracy is also tested as an auxiliary verification. The performance of the algorithm is systematically analyzed by the uniformity of the solution set distribution and convergence, and the computational resource consumption rate is recorded to assess the efficiency. All experiments are executed in the same hardware environment to ensure comparable results. Table 2 displays the outcomes of the experiment.

The data in Table 2 shows that the I-NSGA-II leads in all seven metrics: the IGD value of 0.062 outperforms the weighted single objective of 0.152, the standard NSGA-II of 0.085, and the MOPSO of 0.078. The deconvolution set coverage reaches 89%, which is an improvement of 21% over the standard NSGA-II. The maximum scattering distance of 2.78 and memory footprint of 2.3 GB are both optimal. The number of convergence generations is 80, which is 70 generations less than the weighted method. CPU utilization of 70% and prediction error of 0.07 are both lowest. The outcomes display that the I-NSGA-II has significant advantages in terms of solution set quality, convergence speed and computational efficiency. Among them, the solution set coverage is improved up to 54% over the worst method.

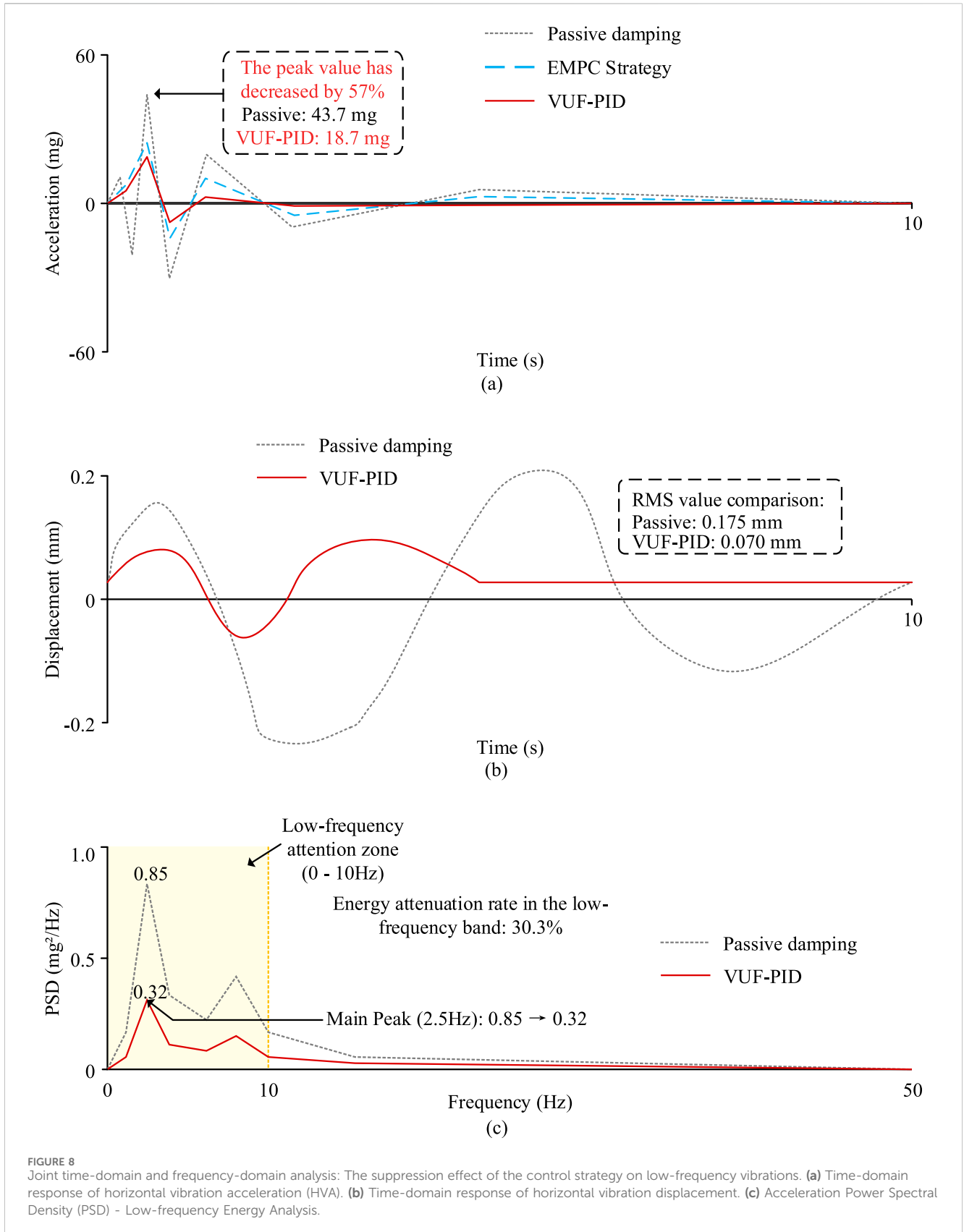
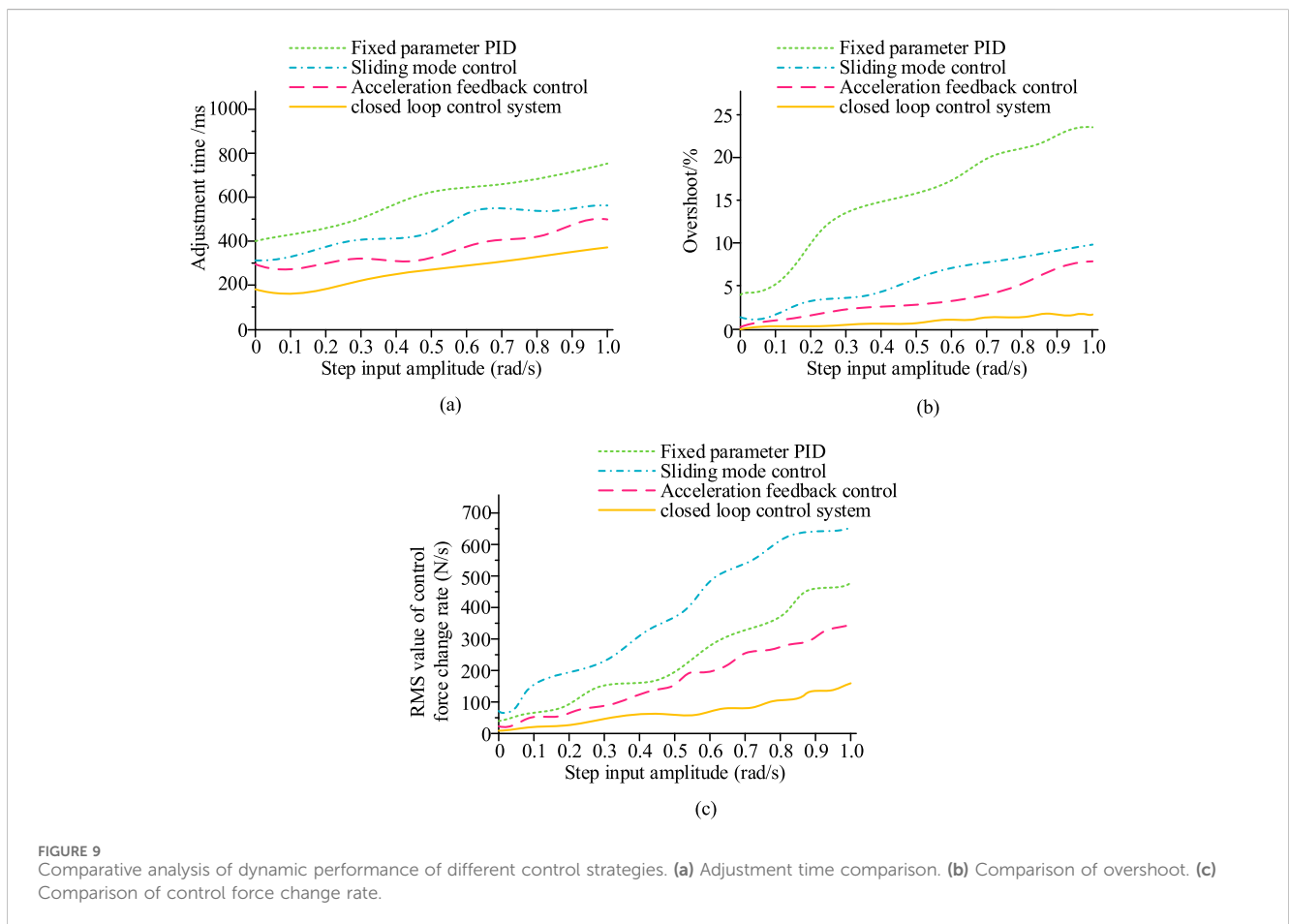


TABLE 2 Comparison of PSS quality and efficiency.

Index	Weighted single objective optimization	Standard NSGA-II	MOPSO	Improved NSGA-II
IGD	0.152	0.085	0.078	0.062
Solution set coverage/%	35	68	72	89
Maximum dispersion distance	1.25	2.10	2.35	2.78
Solution set convergence algebra	150	120	100	80
CPU utilization/%	85	78	82	70
Memory usage	3.2	2.8	3.0	2.3
Prediction error of BPNN	0.18	0.12	0.10	0.07



To verify the dynamic response capability of the system, the study compares four methods, namely, fixed-parameter PID, sliding-mode control, acceleration feedback control and the CLC system proposed in the study. The experiment is based on digital signal processing and control engineering platforms. The step response characteristics of each control strategy are tested at a sampling frequency of 1 kHz. The system’s dynamic performance is evaluated using three key indexes: regulation time, overshoot amount, and control force rate of change. Figure 9 displays the test findings.

Figure 9a shows that the CLC maximum magnitude regulation time is 56% faster than the fixed parameter PID and 40% and 36%

faster than the sliding mode and acceleration feedback, respectively. Figure 9b shows that the overshoot is only 1.4%, which is 94%, 80% and 77% lower than fixed parameter PID, sliding mode and acceleration feedback, respectively. Figure 9c shows that the control force change rate of 171 N/s is 62%, 75, and 50% lower than the three, respectively. The outcomes display that the CLC has significant advantages in three aspects: regulation time, overshooting amount, and control force change rate. These results suggest that the proposed framework achieves lower control force variation, improved energy efficiency, and higher multi-objective coordination without increasing control

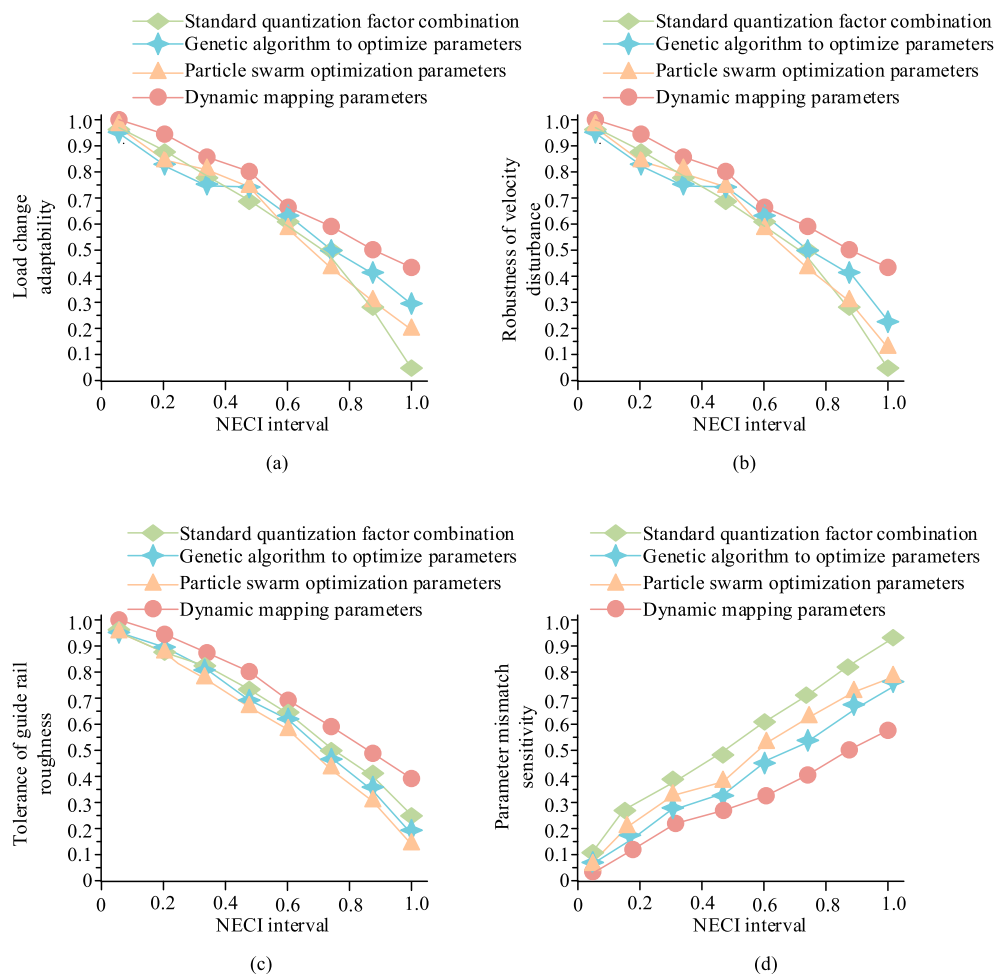


**FIGURE 10** Comparative analysis of system robustness. **(a)** Comparison of load change adaptability. **(b)** Comparison of robustness of velocity disturbance. **(c)** Tolerance comparison of guide rail roughness. **(d)** Parameter mismatch sensitivity comparison.

complexity compared with typical NSGA-II-based fuzzy PID or neural-network-based PID controllers reported in the literature. To verify the robustness of the system, the study compares standard quantization factor combination, genetic algorithm to optimize parameters, particle swarm optimization parameters, and dynamic mapping parameters. The experiment adopts Monte Carlo method to randomly generate 100 sets of working condition parameters. Moreover, it comprehensively evaluates the stability performance of the system under extreme working conditions through four indicators: load change adaptability, robustness of velocity disturbance, tolerance of guide rail roughness, and parameter mismatch sensitivity. Figure 10 displays the test findings.

Figure 10a shows that the adaptive index of dynamic mapping parameters is nearly 1 and fluctuates minimally in all NECI intervals, and the standard quantization factor decreases significantly in high NECI intervals. Figure 10b shows that the method remains highly robust under extreme operating conditions, and the other methods decrease rapidly with increasing NECI. Figure 10c shows that it is significantly better in the middle and high NECI intervals. Figure 10d confirms that the method has the lowest parameter

mismatch sensitivity and the standard quantization factor is significantly more sensitive in the high NECI interval. The results show that dynamic mapping parameters exhibits optimal robustness in all extreme conditions, and the performance of other methods is significantly degraded in the high NECI interval. To verify the superiority of the overall scheme of the study, the proposed integrated control method is compared with three representative commercial HSE vibration control technologies (Commercial Technique A: traditional PID-based active damping system; Commercial Technique B: semi-active electromagnetic damping system; Commercial Technique C: hydraulic active control system) along with EMPC method, acceleration feedback, and SMC. The experiment is carried out in the actual elevator tower of 10-story station for 200 round trips under standardized operational conditions. In accordance with ISO 2631 standards, it measures ride comfort and evaluated multiple core indicators simultaneously: energy consumption index, control equipment complexity, mean time between failures, dynamic parameterization response time, and additional commercial viability metrics, including initial investment cost and installation cycle requirements. Table 3 displays the test results.

TABLE 3 Comprehensive performance comparison of vibration control technologies.

Evaluation metric	Proposed method	Commercial tech A	Commercial tech B	Commercial tech C	EMPC method	Acceleration feedback	SMC
Multi-objective cooperation degree	0.92	0.78	0.85	0.82	0.87	0.80	0.83
Energy consumption index (9%)	75	100	95	110	100	92	98
Control equipment complexity (components)	8	15	18	22	18	12	14
Mean time between failures (hours)	1,200	500	800	600	500	700	650
Dynamic response time (ms)	25	45	35	50	95	40	30
Emergency braking smoothness ( $m/s^2$ )	1.6	2.2	1.9	2.4	2.1	1.8	2.5

TABLE 4 Comparison of performance indicators of elevator control systems under different disturbances.

Disturbance type	Disturbance amplitude	RMS acceleration ( $m/s^2$ )	RMS displacement (mm)	Control energy consumption (kJ)	Control force volatility (%)	Gain margin (dB)	Phase margin ( $^\circ$ )
No disturbance	0	0.08	0.15	1.2	5.2	8.5	60
Mass disturbance	$\pm 20\%$	0.10	0.18	1.3	6.1	8.3	59
Stiffness disturbance	$\pm 20\%$	0.09	0.17	1.25	5.5	8.4	61
Damping disturbance	$\pm 30\%$	0.12	0.19	1.4	7.2	8.1	58
Incremental disturbance	$\pm 10\%$	0.11	0.16	1.35	6.5	8.2	60
External disturbance	Sudden increase in load	0.13	0.21	1.5	8.0	8.0	57

In Table 3, the integrated control method proposed in this study demonstrates significant advantages in multiple key performance indicators. The multi-objective cooperation degree reaches 0.92, which is significantly better than the range of 0.78–0.85 of traditional business technologies. The energy consumption index reduces to 75%, saving 25% energy compared to the benchmark value. The control device has been significantly simplified, reducing its complexity from ten components to eight, compared to the EMPC method. The average mean time between failures has increased to 1,200 h, achieving a reliability level more than twice that of traditional technologies. The dynamic response time is only 25 ms, which is nearly four times faster than the 95 ms response speed of EMPC. Although  $1.6\text{--}2.5\text{ m/s}^2$  is slightly lower than SMC's  $2.5\text{ m/s}^2$  in terms of emergency braking smoothness, it still outperforms other commercial technologies. The results demonstrate comprehensive breakthroughs in energy efficiency, reliability, response speed, and system integration with this control scheme. All performance indicators improved in a coordinated manner, with no obvious shortcomings emerging, which demonstrates its excellent engineering application value.

To verify the stability and robustness of the proposed control method in the presence of different disturbances, an experiment is conducted on a standard hardware platform consisting of a 10-story elevator test tower. This tower integrates a MEMS accelerometer and a photoelectric encoder that monitor the vibration acceleration and displacement of the guide shoe in real time. The experiment disturbed the key parameters of the system, including  $\pm 20\%$  of the EC mass,  $\pm 20\%$  of the guide rail system stiffness,  $\pm 30\%$  of the damping coefficient,  $\pm 10\%$  of the PID controller gain, and external load disturbance. For each group of disturbances, the system's RMS acceleration, displacement, control energy consumption, and control force fluctuation are recorded. Stability and robustness analyses, such as gain margin and phase margin, are also conducted. Through simulation or experimental data, compare the control effects and system stability under different disturbances, and analyze the impact of disturbances on control performance. The experimental results are shown in Table 4.

As shown in Table 4, the system exhibits optimal performance under undisturbed reference conditions, with an RMS acceleration of  $0.08\text{ m/s}^2$ , a displacement of 0.15 mm, a control energy consumption of 1.2 kJ, a control force fluctuation of 5.2%, and

stability margins of 8.5 dB and 60°. System performance degrades to varying extents after parameter disturbances are introduced. The most pronounced impact is caused by sudden external load disturbance, which increases the RMS acceleration to 0.13 m/s<sup>2</sup> and reduces the stability margins to 8.0 dB and 57°. A ±30% damping disturbance also leads to noticeable performance degradation. Meanwhile, the influence of a ±20% mass disturbance and a ±10% gain disturbance is more significant than that of a ±20% stiffness disturbance. Under all disturbance conditions, the gain margin and phase margin remain positive, indicating that the closed-loop system maintains stability under parameter uncertainties. Although a strict Lyapunov-based stability proof is not provided, the proposed control system can be equivalently regarded as a closed-loop structure with bounded time-varying gains. As shown in Table 4, the parameter perturbation and stability margin verification results demonstrate that the proposed control strategy is robust from an engineering perspective because sufficient gain and phase margins are preserved over a wide range of uncertainties.

## 5 Conclusion

This study successfully overcame the challenge of HV in HSE cars. It proposed an intelligent control method that integrated an I-NSGA-II with a uVUF-PID controller. To address the identified limitation regarding theoretical robustness, the conclusion was reinforced by emphasizing the importance of a Lyapunov-based stability analysis in future work. This approach provided a clear path for achieving formal guarantees of system stability under varying operating conditions.

The core innovation lies in the enhanced synergy between the optimization algorithm and the control strategy. The I-NSGA-II was optimized using an adaptive crossover-variance operator and a dynamic congestion threshold. This explains its superior convergence characteristics, evidenced by a 35% reduction in the number of required generations compared to the standard NSGA-II. This optimized algorithm was combined with a 3-7-2 structured BPNN to create an efficient “sensing-prediction-control” closed-loop system.

Experimental results under 6 m/s conditions demonstrated the method's exceptional performance: a 57% reduction in HVA (to 18.7 mg), a 60% reduction in displacement (to 0.070 mm), and a low-frequency energy attenuation rate of 30.3%. This was 12.5% higher than the EMPC method. The dynamic mapping parameters method exhibited optimal robustness in extreme conditions, with the load adaptability index stable and close to 1. The integrated solution achieved a high degree of multi-objective cooperation (0.92), alongside a 25% reduction in energy consumption, simplified control equipment (8 components), and an increased mean time between failures (1,200 h).

The causal link between algorithmic mechanisms and control performance was clearly established. The vibration suppression improvements were attributed to the VUF-PID's adaptive parameter adjustment, enabled by its 49-rule fuzzy inference system and dynamic universe scaling, which effectively handled nonlinear vibration characteristics. The study thus provided a

comprehensive solution that overcame the adaptability limitations of traditional methods.

Despite its success, there are still limitations, such as the lack of a theoretical stability proof and delays in the real-time response. Future work will focus on developing formal Lyapunov stability proofs, optimizing dynamic parameter tuning with deep reinforcement learning, and exploring digital twin technology for predictive vibration control in multi-car elevator systems.

## Data availability statement

The original contributions presented in the study are included in the article/supplementary material, further inquiries can be directed to the corresponding author.

## Author contributions

LW: Conceptualization, Investigation, Writing – original draft. RZ: Methodology, Validation, Writing – review and editing. YG: Visualization, Writing – review and editing.

## Funding

The author(s) declared that financial support was not received for this work and/or its publication.

## Conflict of interest

The author(s) declared that this work was conducted in the absence of any commercial or financial relationships that could be construed as a potential conflict of interest.

## Generative AI statement

The author(s) declared that generative AI was not used in the creation of this manuscript.

Any alternative text (alt text) provided alongside figures in this article has been generated by Frontiers with the support of artificial intelligence and reasonable efforts have been made to ensure accuracy, including review by the authors wherever possible. If you identify any issues, please contact us.

## Publisher's note

All claims expressed in this article are solely those of the authors and do not necessarily represent those of their affiliated organizations, or those of the publisher, the editors and the reviewers. Any product that may be evaluated in this article, or claim that may be made by its manufacturer, is not guaranteed or endorsed by the publisher.

## References

- Chen, L., Xue, K., Li, J., Li, R., Yu, N., Sun, Q., et al. (2023). Q-DDCA: decentralized dynamic congestion avoid routing in large-scale quantum networks. *IEEE/ACM Trans. Netw.* 32 (1), 368–381. doi:10.1109/TNET.2023.3285093
- Fan, W., Zhang, S., Wu, Z., Liu, Y., and Yu, J. (2024). Vibration control of the rail grinding vehicle with abrasive belt based on structural optimization and lightweight design. *Chin. J. Mech. Eng.* 37 (3), 311–337. doi:10.1186/s10033-024-01043-3
- Gao, J., Wang, C., Hao, Y., Liang, X., and Zhao, K. (2022). Prediction of TC11 single-track geometry in laser metal deposition based on back propagation neural network and random forest. *J. Mech. Sci. Technol.* 36 (3), 1417–1425. doi:10.1007/s12206-022-0229-0
- Hasanvand, M., Nooshyar, M., Moharamkhani, E., and Selyari, A. (2023). Machine learning methodology for identifying vehicles using image processing. *AIA* 1 (3), 170–178. doi:10.47852/bonviewAIA3202833
- He, Q., Jia, T., Zhang, R., and Liu, L. (2022). Adaptive sliding mode control with fuzzy adjustment of switching term based on the Takagi-Sugeno model for horizontal vibration of the high-speed elevator cabin system. *Proc. Institution Mech. Eng. Part C J. Mech. Eng. Sci.* 236 (9), 4503–4519. doi:10.1177/09544062211053191
- Jiang, G., Zang, H., Xiong, Y., Shen, Y., Guo, Z., Yang, Y., et al. (2025). Design and vibration reduction performance analysis of a 6-DOF nonlinear vibration isolation platform by employing bio-inspired multi-joint X-structure. *Nonlinear Dyn.* 113 (16), 21119–21150. doi:10.1007/s11071-025-11256-3
- Li, H., He, Q., Li, L., and Liu, L. X. (2023). Research on optimal fast terminal sliding mode control of horizontal vibration of high-speed elevator car system. *Trans. Can. Soc. Mech. Eng.* 48 (2), 183–202. doi:10.1139/tcsme-2023-0055
- Li, H., Qiu, L., Wang, J., Zhang, L., Tan, J., and Zhu, L. (2024). A horizontal vibration prediction method of high-speed elevator based on transferred-digital twin model. *Proc. Institution Mech. Eng. Part C J. Mech. Eng. Sci.* 238 (17), 8603–8618. doi:10.1177/09544062241245192
- Lian, L. (2022). Main steam temperature control based on variable universe fuzzy dynamic matrix control. *Therm. Eng.* 69 (10), 763–778. doi:10.1134/S0040601522100044
- Murugapoopathi, S., Ramachandran, T., and Surendarnath, D. S. (2023). Optimization of engine parameters using NSGA II for the comprehensive reduction of emissions from VCR engine fuelled with ROME biodiesel. *Environ. Sci. Pollut. Res.* 30 (22), 61162–61176. doi:10.1007/s11356-022-19752-4
- Qin, G., and Yang, Z. (2021). Time-varying characteristics of guide roller-rail contact stiffness of super high-speed elevator under aerodynamic load. *J. Braz. Soc. Mech. Sci. Eng.* 43 (10), 1–14. doi:10.1007/s40430-021-03190-3
- Shi, Q., Wang, Z., Ke, X., Wang, Z., Gao, Q., Fan, Y., et al. (2023). Multiobjective trajectory optimization of the wall-building robot based on RBF-NSGA-II in an uncertain viscoelastic contact environment. *J. Field Robotics* 40 (8), 1964–1995. doi:10.1002/rob.22235
- Wang, S., Wang, R., Xia, Y., Sun, Z., and Zhang, J. (2021). Multi-objective aerodynamic optimization of high-speed train heads based on the PDE parametric modeling. *Struct. Multidiscip. Optim.* 64 (3), 1285–1304. doi:10.1007/s00158-021-02916-0
- Wei, S., Cao, Z., Zhang, Z., Ye, Y., and Liu, L. (2024). Horizontal vibration and control methods in high-speed elevator car systems: a review. *Mechatronics Technol.* 1 (1), 23–24. doi:10.55092/mt20240004
- Wu, Y., Chen, E., Ferguson, N. S., He, Y., Wei, H., and Lu, Y. (2023). An optimization method for vibration suppression and energy dissipation of an axially moving string with hybrid nonclassical boundaries. *J. Mech. Sci. Technol.* 37 (3), 1177–1187. doi:10.1007/s12206-023-0204-4
- Yang, Y., He, Z., Shi, Z., and Xiong, X. H. (2022). Multi-objective aerodynamic optimization of a high-speed train head shape based on an optimal kriging model. *J. Appl. Fluid Mech.* 15 (3), 803–813. doi:10.47176/jafm.15.03.33183
- Zhang, R., Ge, Q., and Zhang, H. (2024). Intelligent vibration control for ultra-high-speed elevators: a type 2 variable universe fuzzy neural network method with input saturation. *Mech. Based Des. Struct. Mach.* 52 (7), 4173–4190. doi:10.1080/15397734.2023.2223706
- Zhang, S., Zhang, Q., Su, X., Zhao, Z., He, Q., and Meng, L. (2025). Research on explicit model predictive control method for horizontal vibration of high-speed elevator car system. *J. Braz. Soc. Mech. Sci. Eng.* 47 (1), 1–19. doi:10.1007/s40430-024-05349-0
- Zhao, X., Wang, C., Ji, H., Qiu, J., and Cheng, L. (2024). Vibration reduction by a partitioned dynamic vibration absorber with acoustic black hole features. *Chin. J. Mech. Eng.* 37 (1), 1–15. doi:10.1186/s10033-024-01049-x
- Zhao, M., Qin, C., Tang, R., Tao, J., Xu, S., and Liu, C. (2024). An acceleration feedback-based active control method for high-speed elevator horizontal vibration. *J. Vib. Eng. and Technol.* 12 (2), 1943–1956. doi:10.1007/s42417-023-00955-z
- Zhao, Z., Zhang, R., Su, X., Zhang, S., and He, Q. (2024). Research on anti-saturation horizontal vibration model and neural network adaptive integral terminal sliding mode control strategy for high-speed elevator car system. *Int. J. Robust Nonlinear Control* 34 (18), 12286–12311. doi:10.1002/rnc.7618

## Nomenclature

<b>NSGA-II</b>	Multi-objective evolutionary optimization algorithm (Nondominated Sorting Genetic Algorithm II)
<b>VUF-PID</b>	Adaptivefuzzy logic controller with dynamic domain adjustment (Variable Universe Fuzzy Proportional-Integral-Derivative)
<b>BPNN</b>	Artificial neural network with error backpropagation training (Back Propagation Neural Network)
<b>MOO</b>	Optimization involving multiple conflicting objectives (Multi-Objective Optimization)
<b>HSE</b>	Elevator system operating at speeds above 5 m/s (High-Speed Elevator)
<b>HV</b>	Lateral oscillation of elevator car during operation (Horizontal Vibration)
<b>HVA</b>	Acceleration magnitude of lateral vibrations (Horizontal Vibration Acceleration)
<b>RMS</b>	Statistical measure of signal magnitude (Root Mean Square)
<b>EMPC</b>	Advanced control method using explicit solution (Explicit Model Predictive Control)
<b>SMC</b>	Robust control technique with sliding surface (Sliding Mode Control)
<b>ECR</b>	Derivative component of control error (Error Change Rate)
<b>CLC</b>	Feedback control system with continuous adjustment (Closed-Loop Control)
<b>MEMS</b>	Miniaturized sensor and actuator technology (Micro-Electro-Mechanical Systems)
<b>TOPSIS</b>	Multi-criteria decision making method (Technique for Order Preference by Similarity to Ideal Solution)
<b>PSS</b>	Collection of nondominated optimal solutions (Pareto Solution Set)